Facile in-situ construction of highly dispersed nano zero-valent iron modified black TiO$_2$ Z-scheme recyclable heterojunction with highly efficient visible-light-driven photocatalytic activity

Xi Wu [a], Xiangyu Wang [a,*], Yu Xie [a], Nanqi Ren [b,*], Jun Ma [b], Ping Ning [a]

[a] Faculty of Environmental Science and Engineering, Kunming University of Science and Technology, Kunming 650500, China
[b] School of Municipal and Environmental Engineering, Harbin Institute of Technology, Harbin 150090, China

A B S T R A C T

This research provides a innovatively designed mechanism of activating the passivation layer on Fe^0 surface as semiconductor to construct a Z-scheme heterojunction in-situ for high-efficiency environmental remediation. Aggregation and passivation of Fe^0 and poor visible-light absorption of TiO$_2$ were simultaneously improved by the facile synthesis of a recyclable Fe^0@black-TiO$_2$ Z-scheme heterojunction without high-temperature hydrogen atmosphere. The results showed that tetracycline (TC) degradation efficiency with Fe^0@black-TiO$_2$ was 1.23 and 2.63 times higher than that of pristine Fe^0 and black-TiO$_2$, respectively. The superior degradation arose from strong reduction ability of highly dispersed Fe^0 and in-situ constructed Z-scheme heterojunctions. High dispersion of Fe^0, construction of the heterojunction, enhanced photodegradability of Fe^0@black-TiO$_2$ were systematically elucidated by multiple characterization techniques. Furthermore, photodegradation pathways of TC based on the role of •O$_2^-$ and •OH were identified. Our results have provided the necessary inspiration and guidance for the development and application prospect of Fe^0@black-TiO$_2$ in environmental remediation.

1. Introduction

Tetracycline (TC), as a class of highly effective antibacterial drugs, is widely used to treat infections of humans and animals [1]. However, considerable amounts of studies have demonstrated that a large proportion of TC is difficult to be absorbed completely by water body, resulting in its excessive discharge into natural environment [1–3]. To make matters worse, traditional sewage treatment plants cannot effectively eliminate TC, leading to the widespread existence of resistant bacteria and resistance genes [2,4]. It poses a serious threat to the health of humans and animals, on the other hand, it is not conducive to the balanced development of ecosystem [2,5].

Nano zero-valent iron (nZVI), with strong reduction ability and environmentally harmless, showing strong adsorption and reactivity to organic pollutants such as antibiotics, is frequently applied in the environmental remediation process [6,7]. However, the aggregation tendency and passivation problem of nZVI have become two key factors limiting its large-scale application [7–10]. In view of this, researchers have adopted several methods to overcome these drawbacks, such as surface modification, metal doping and support loading [11–15]. The aggregation of nZVI could be decreased to some extent due to the electrostatic effect and steric hindrance of surface modifiers. But it also inevitably affected the catalytic activity of nZVI due to the contact between Fe^0 and pollutants was restricted by surface modifiers [12]. As for metal doping, the combination of Fe^0 and Pd, Ni, Cu, Mn, etc. to form bimetallic nanoparticles could well inhibit the formation of a passivation layer on its surface, which ensured the stability of Fe^0-based material, the aggregation of metal particles was yet unavoidable [16–19].

Therefore, support loading is expected as a promising method to solve the problems of particle aggregation and passivation layer formation, simultaneously. In recent years, photocatalytic technology has been widely concerned by researchers worldwide due to its high efficiency and environmental friendliness. Among a variety of photocatalytic materials, titanium dioxide has become a popular material in the field of photocatalytic degradation of organic pollutants, which is attributed to its low cost and excellent photocatalytic stability [20–22]. Zhou et al. reported a 95% TC (40 mg·L^{-1}) removal rate after 60 min UV irradiation using nanosized TiO$_2$ (P25, 40 mg) [23]. Lin et al. compared the photodegradation of TC (10 mg·L^{-1}) over TiO$_2$ (20 mg) within 120 min under visible-light and UV light irradiation, respectively [24].
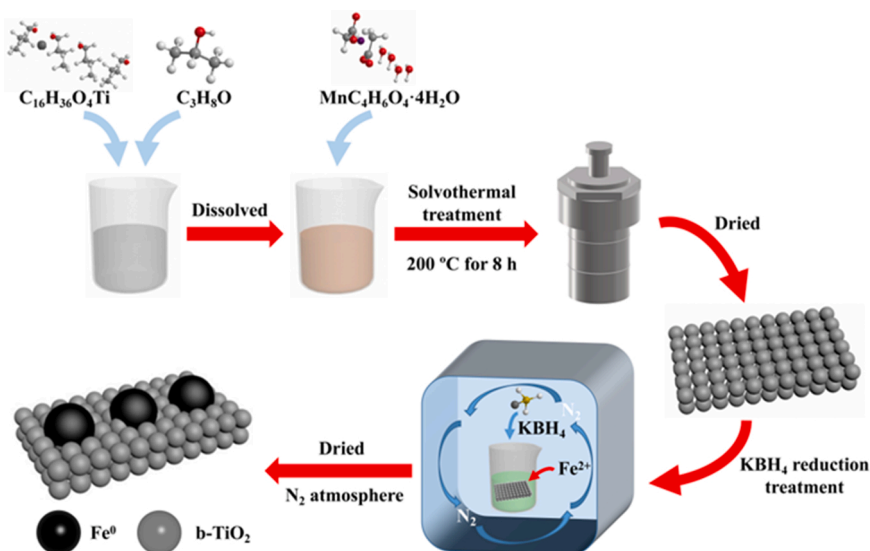
Fig. 1. Schematic illustration of the preparation of Fe^0@b-TiO_2.

Studies have shown that the photocatalytic degradation of TC reached 94.8% under UV (λ = 350 nm) irradiation, surprisingly, the photo-degradation efficiency of TC could reach 41.9% even under visible-light (λ = 600 nm) irradiation. Nevertheless, low utilization of visible-light and wide band gap are still the main non-negligible drawbacks for TiO_2. Up to date, an ideal method to improve its optical properties is the preparation of black TiO_2 (b-TiO_2). More recently, a large number of studies have confirmed that b-TiO_2 has a narrower band gap and stronger visible-light absorption compared to TiO_2 [25–29]. Feng et al. demonstrated that the presence of Ti^{3+} or oxygen vacancies (OVs) in the bulk phase extended the light response range of TiO_2 from UV to visible-light [27]. As was also reported by Naldoni et al., the band gap narrowing of b-TiO_2 was ascribed to the formation of Ti^{3+} or OVs in the bulk [28]. Pang et al. also confirmed the same conclusion [29]. However, due to the rapid recombination of photo-generated electrons and holes, an ideal photocatalytic efficiency is still not achieved for b-TiO_2.

Consensus holds that nZVI easily reacts with oxygen and water in the liquid phase to produce iron oxide (Fe_2O_3) [30,31]. The produced Fe_2O_3 is the main composition of the passivation layer of Fe^0. It is usually regarded as an unwanted or even inhibitory substance to the Fe^0-based catalytic reaction [32–34]. In spite of this, Fe_2O_3 can be used as a typical semiconductor material that can absorb a broad spectrum of sunlight in photocatalysis [35]. Herein, for the first time, we propose a innovative technology of converting the passivation layer as a semiconductor to enhance the activity of Fe^0-based composite. After being combined with the b-TiO_2 support, it is expected to form a heterojunction, which not only restrains the recombination of photo-generated electrons and holes, but also facilitates the dispersion between Fe^0 particles and uses the passivation layer instead of being adversely affected by it, achieving dramatically enhanced photocatalytic performance. So far, although b-TiO_2 has been proved to be a new-type of high-efficiency visible-light material, its TC photodegradation activity after cooperation with Fe^0 has not been reported, and whether the combination of the passivation layer and b-TiO_2 can turn the disadvantage into the advantage has not yet been explored.

The main objective of this research is to investigate the feasibility of applying an innovative mechanism of transforming the passivation layer that adversely affected the activity of nZVI into activator for the enhancement of photocatalytic property of b-TiO_2 supported nZVI composite (Fe^0@b-TiO_2). To the best of our knowledge, this is the first report of a complete new approach of constructing Fe^0@b-TiO_2 Z-scheme heterojunction nanocomposite with highly dispersed Fe^0 and enhanced catalytic performance and its application in treatment of

tetracycline wastewater. In particular, a facile solvothermal method was employed for synthesis of b-TiO_2 with a narrow band gap and enhanced visible-light photocatalytic ability. It was also worth noting that the high dispersion among Fe^0 particles was induced by the combination of Fe^0 and b-TiO_2. Furthermore, the combination promoted the in-situ formation of a Z-scheme heterojunction between the passivation layer and b-TiO_2. In addition, the morphology, catalytic activity and stability, kinetics and optical properties of Fe^0@b-TiO_2 were systematically revealed. The reaction pathways of TC photodegradation were proposed, more importantly, the in-situ construction and reaction mechanism of the Z-scheme heterojunction were confirmed and investigated deeply.

2. Materials and methods

2.1. Materials

Tetrabutyl titanate ($C_{16}H_{36}O_4Ti$) and potassium borohydride (KBH_4) were obtained from Chron Chemicals Co., Ltd (Chengdu, China). Tetracycline ($C_{22}H_{24}N_2O_8$), ferrous sulfate heptahydrate ($FeSO_4·7H_2O$), methanol (CH_4O), isopropanol (C_3H_8O), ethanol (C_2H_6O) and acetone (C_3H_6O) were purchased from Jinsui Bio-Technology Co., Ltd (Shanghai, China), ZhiYuan Reagent Co., Ltd (Tianjin, China), YongDa Chemical Reagent Co., Ltd (Tianjin, China), FuChen Chemical Reagents Factory (Tianjin, China), AnTe Food Co., Ltd (Anhui, China) and Shan-Dian Co., Ltd (Kunming, China), respectively. Manganese acetate tetrahydrate ($MnC_4H_6O_4·4H_2O$), p-benzoquinone ($C_6H_4O_2$, p-BQ), dimethyl sulfoxide (C_2H_6OS, DMSO), ammonium oxalate monohydrate (($NH_4)_2C_2O_4·H_2O$, AO) were acquired from Aladdin Biochemical Technology Co., Ltd (Shanghai, China). Ultrapure water (UPW) with a resistivity of 18.25 MΩ·cm was used in all experiments and all other reagents were used as received without any further purification.

2.2. Preparation of Fe^0@b-TiO_2

2.2.1. b-TiO_2

b-TiO_2 was synthesized by a solvothermal method (Fig. 1). Specifically, 3.4 g of tetrabutyl titanate was dissolved in 25 mL of isopropanol, stirring is continued for a further 10 min 0.1226 g of manganese acetate tetrahydrate was hydrolyzed by 25 mL of H_2O under continuous stirring. Then, the manganese-containing solution was quickly poured into the former solution, followed by further stirring for 30 min to form a homogeneous sol. Subsequently, the sol was transferred into a 100 mL
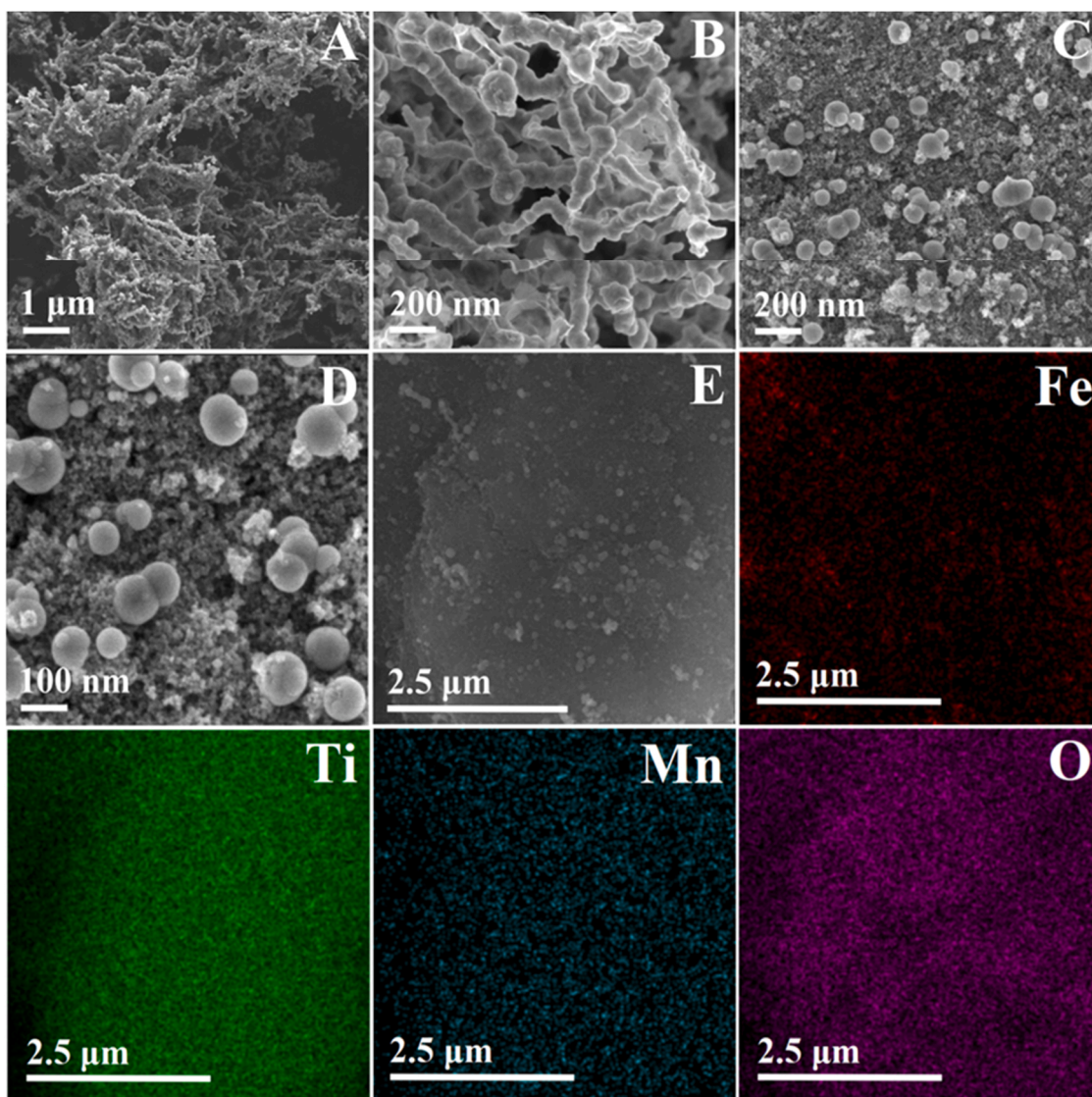
Fig. 2. SEM images of (A-B) bare Fe^0 and (C-D) Fe@Ti-2. (E) Elemental mapping (Fe, Ti, Mn, O) of the as-prepared Fe@Ti-2.

Teflon-lined stainless-steel autoclave and maintained at 200 °C for 8 h. Finally, the products were naturally cooled overnight, and the resulting products were filtered, washed for 3 times with UPW, and dried overnight at 80 °C in an oven to obtain b-TiO$_2$ particles.

2.2.2. Fe^0@b-TiO$_2$

Fe^0@b-TiO$_2$ was prepared by a facile chemical reduction method in an anaerobic chamber (Fig. 1). Briefly, a certain amount of b-TiO$_2$ was firstly added to the aqueous solution of FeSO$_4$.7H$_2$O and magnetically stirred for 10 min. Then, excess KBH$_4$ solution was slowly titrated into the previous solution to ensure not only the complete reduction of Fe^{2+}, but also the homogeneous dispersion of Fe^0 and its stable anchor on the surface of b-TiO$_2$. After titration, the mixture was continuously stirred for 30 min, and washed for 3 times with UPW, ethanol, and acetone in sequence while being filtered. Finally, the as-prepared composites were dried and stored at room temperature in an anaerobic drying oven. In order to obtain the optimal activity, catalysts with different mass ratios of FeSO$_4$.7H$_2$O to b-TiO$_2$ (1:2, 1:1 and 2:1) were synthesized and denoted as Fe@Ti-1, Fe@Ti-2 and Fe@Ti-3, respectively. In contrast, Fe^0 was prepared by the chemical reduction method without the presence of b-TiO$_2$. In addition, Fe@Ti-2 after dark reaction for 30 min and the physical mixture of Fe^0 and b-TiO$_2$ (same mass ratio as Fe@Ti-2) were named as Fe$_2$O$_3$@Ti-2 and Fe^0+b-TiO$_2$, respectively.

2.3. Photocatalytic experiment

The performance of photocatalytic degradation of TC over Fe^0@b-TiO$_2$ was evaluated by a photochemical reactor (300 W xenon lamp, 420 nm cut-off filter, ZQ-GHX-V, China). Prior to visible-light irradiation, 7 mg of Fe^0@b-TiO$_2$ sample was dispersed into 60 mL of 30 mg·L^{-1} TC solution and magnetically stirred for 30 min under dark conditions to achieve an adsorption-desorption equilibrium. After that, the visible-light source was turned on for the photodegradation reaction. At a given time interval, a 1 mL aliquot was extracted, filtered and diluted 10 times sequentially. The content of TC in the sample was measured using a UV–vis spectrophotometer (UV-1800PC, China) at an absorption wavelength of 357 nm. The degradation efficiency of TC (DE, %) was calculated with the following equation:

$$DE\ (\%) = [(C_0 - C_t) / C_0] \times 100 \tag{1}$$

where C_0 represents the initial concentration of TC, and C_t is the concentration of TC at time t (min). In addition, the photocatalytic stability of Fe^0@b-TiO$_2$ was examined by conducting recycling experiments with a total of 5 cycles.
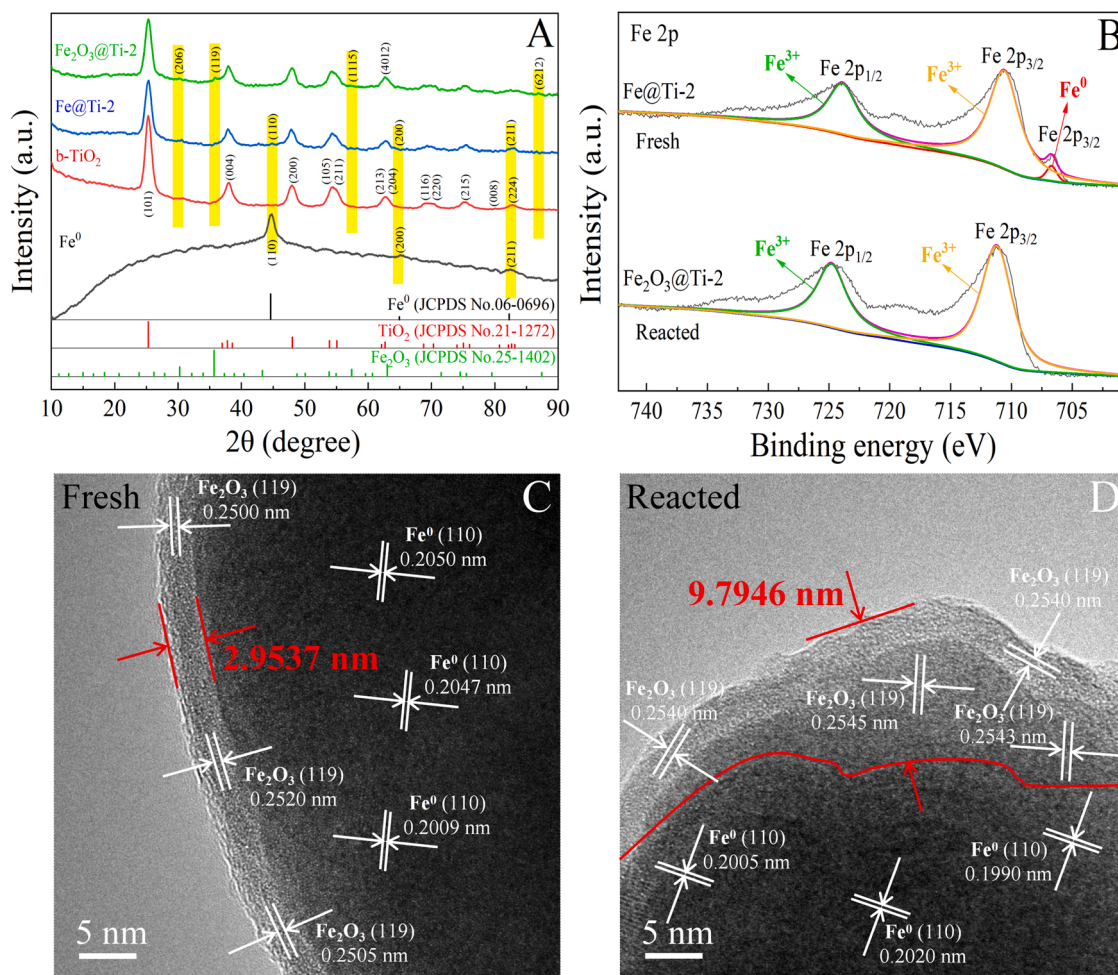
Fig. 3. (A) XRD patterns of bare Fe^0, b-TiO_2, Fe@Ti-2, Fe_2O_3@Ti-2. (B) Fe 2p XPS spectra of Fe@Ti-2 and Fe_2O_3@Ti-2. TEM images of (C) Fe@Ti-2 (fresh catalyst) and (D) Fe_2O_3@Ti-2 (reacted catalyst).

2.4. Characterization

The morphology and structure of Fe^0 and Fe@Ti-2 were investigated by field-emission scanning electron microscopy (SEM, ZEISS GeminiSEM 300, Germany). The successful synthesis of Fe@Ti-2 and the dispersion of Fe^0 were analyzed by mapping (Oxford X-MAX, England). The BET surface areas of samples were determined by the specific surface area analyzer (BET, Micromeritics TriStar II 3020, America). The crystal phase of single-component materials and composites and the transformation of Fe^0 crystal phase after dark reaction were detected by powder X-ray diffraction (XRD, Bruker D8 ADVANCE, Germany). The structure of Fe@Ti-2 and Fe_2O_3@Ti-2 were analyzed by transmission electron microscopy (TEM, Thermo Fisher TF20, America) and X-ray photoelectron spectroscopy (XPS, Thermo Scientific K-Alpha+, America). The magnetic property of the composite was measured using superconducting quantum interference device (SQUID, Quantum Design MPMS-XL-5, America). The recombination and lifetime of photo-generated carriers were measured by photoluminescence spectra (PL) and time-resolved fluorescence spectra (Olympus FV1000, Japan) with a 320 nm excitation wavelength, respectively. The light absorption region and photo-generated carriers mobility of b-TiO_2 and Fe@Ti-2 were recorded by ultraviolet-visible diffuse reflectance spectra (UV–vis DRS, Shimadzu UV-3600 Plus, Japan) and electrochemical workstation (transient photocurrent response, CHI660E, China), respectively. The band gap and valence band (VB) of Fe_2O_3 and b-TiO_2 were calculated according to Tauc plots and VB-XPS (Thermo Fisher ESCALAB Xi+, America), respectively. Several quenchers (p-BQ, DMSO, AO and

methanol) were employed to identify the key active species driving TC photodegradation. The reactive oxygen species (ROS) and h^+ generated during TC photocatalytic over b-TiO_2 and Fe@Ti-2 were confirmed with electron spin resonance spectroscopy (ESR, JEOL JES-FA200, Japan). The photodegradation paths of TC were recorded by liquid chromatography mass spectrometry (LC-MS, Agilent 1290–6460, America).

3. Results and discussion

3.1. Morphology and structure of the as-prepared catalysts

The detailed morphology and micro-structure of bare Fe^0 and Fe@Ti-2 were observed through SEM and mapping techniques (Fig. 2). The aggregated pristine Fe^0 with chain-like structure is presented in Fig. 2A. Furthermore, the structure is found to be assembled by multiple spherical Fe^0 particles (Fig. 2B). The phenomenon can be attributed to the magnetic effect of iron, which has also been confirmed in many literatures [36–38]. However, it can be seen from Fig. 2C that after Fe^0 is doped with b-TiO_2, these spherical Fe^0 particles exhibit a high degree of dispersion on the b-TiO_2 support by overcoming their own magnetism, which may be due to the steric hindrance and electrostatic repulsion of b-TiO_2 particles [38,39]. As shown in Fig. 2D, compared to bare Fe^0, the dispersed Fe^0 with a particle size less than 100 nm presents a more regular spherical shape and its surface is smoother. The BET surface areas (Table S1) of Fe^0, b-TiO_2 and Fe@Ti-2 are 10.4570 m^2/g, 126.1908 m^2/g, and 138.5637 m^2/g, respectively, indicating a significant improvement in the dispersion of Fe^0. In addition, the fluffy
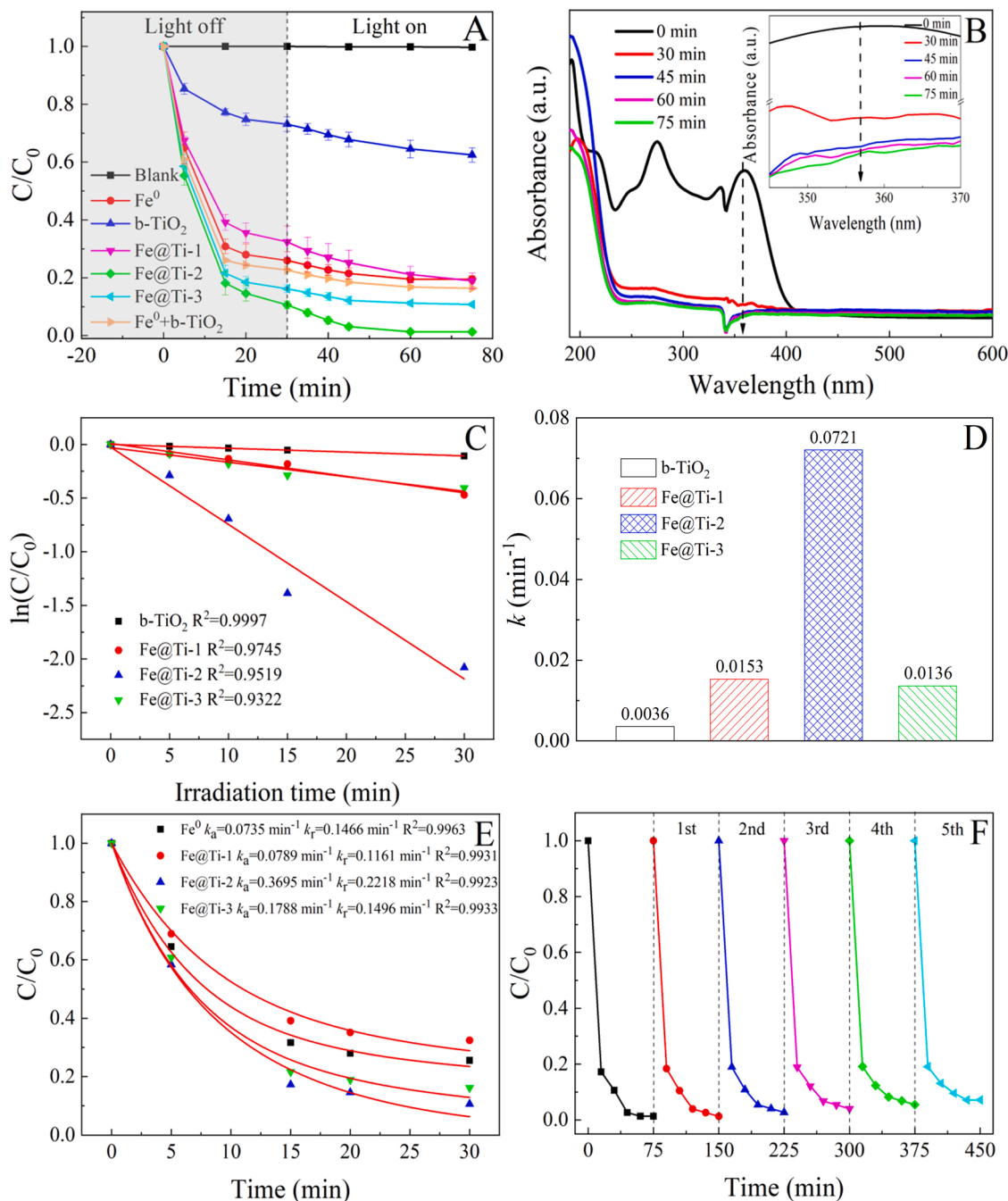
Fig. 4. (A) TC photodegradation activity of the as-synthesized materials. (B) UV–vis absorption spectra of TC over Fe@Ti-2 under different degradation time. (C) The pseudo-first-order kinetics plots and (D) the corresponding reaction rate constant *k*, (E) the modified kinetics plots of the as-synthesized materials. (F) Cycling experiments of TC photodegradation over Fe@Ti-2.

sponge-like structure formed between b-TiO$_2$ particles improves the confinement effect of Fe^0 particles and induces them to be embedded between b-TiO$_2$ particles. Meanwhile, such a structure is also conducive to efficient adsorption of pollutants and exposure of more active centers. As depicted in Fig. 2E, the four elements of Fe, Ti, Mn, and O show a uniform distribution, again indicating that Fe^0 is successfully implanted into the b-TiO$_2$ support. Moreover, the high dispersion of Fe^0 particles on the b-TiO$_2$ support is also further confirmed by the mapping analysis.

The crystal structure of pristine Fe^0, b-TiO$_2$ and Fe@Ti-2, and formation of a new crystal phase of Fe@Ti-2 after dark reaction for 30 min in TC solution were analyzed by XRD technology. As shown in Fig. 3A, the diffraction peaks at $2\theta = 44.7°$, $65.1°$ and $82.4°$ belong to the characteristic peaks of Fe^0 (JCPDS No.06–0696), which are indexed as

its (110), (200), (211) crystal planes, respectively [40,41]. The prominent characteristic peaks also indicate the high crystallinity of bare Fe^0 sample. The sharp diffraction peaks located at $2\theta = 25.2°$, $37.9°$, $48.0°$, $54.1°$, $55.0°$, $62.3°$, $62.8°$, $68.8°$, $70.3°$, $75.1°$, $80.5°$ and $82.7°$ are indexed to (101), (004), (200), (105), (211), (213), (204), (116), (220), (215), (008), (224) crystal planes of anatase TiO$_2$ (JCPDS No.21–1272), respectively, reflecting the unaltered crystal structure and high crystallinity of b-TiO$_2$ as its color changed [42,43]. Compared with high-purity black anatase TiO$_2$, the XRD pattern of Fe@Ti-2 shows sharp characteristic diffraction peaks of anatase TiO$_2$, indicating that the crystal structure of black anatase TiO$_2$ is not destroyed after Fe^0 loading. More importantly, the characteristic diffraction peak of Fe^0 is also observed in Fe@Ti-2 with weakened peak intensity and increased peak

Table 1
Comparison of photocatalytic activity and key experimental parameters under different catalysts.

Catalyst	Dosage (mg)	C_0 (mg/L)	Volume (mL)	Time (min)	Removal (%)	Light source	Ref.
CuInS$_2$/g-C$_3$N$_4$	50	10	100	60	83.7	300 W xenon lamp ($\lambda > 420$ nm)	[45]
ZIF-8@TiO$_2$	60	100	100	40	Nearly 90	300 W xenon lamp	[46]
Mn-doped BiOCl	100	20	100	15	96	300 W xenon lamp ($\lambda > 420$ nm)	[47]
CoP/HCCN	40	10	100	120	96.7	500 W xenon lamp ($\lambda > 420$ nm)	[48]
AgBr/CuBi$_2$O$_4$	50	10	100	60	90	300 W xenon lamp ($\lambda > 420$ nm)	[49]
CDs-CoO	50	10	100	60	87	300 W xenon lamp ($\lambda > 420$ nm)	[50]
γ-Fe$_2$O$_3$/b-TiO$_2$	30	10	100	50	99.3	300 W Xe lamp with an AM 1.5 filter	[51]
TiO$_2$	20	10	100	120	56.7	300 W xenon lamp ($\lambda = 500$ nm)	[24]
Black anatase-TiO$_2$	20	10	100	240	66.2	1000 W xenon lamp ($\lambda > 400$ nm)	[52]
Fe^0@b-TiO$_2$	7	30	60	30	98.67	300 W xenon lamp ($\lambda > 420$ nm)	This work

width. It can be interpreted as the successful preparation of Fe@Ti-2, and Fe^0 exhibited a high and uniform dispersion on the b-TiO$_2$ support [44]. This result is consistent with the conclusion drawn in SEM image. As for Fe$_2$O$_3$@Ti-2, it can be seen that even after 30 min of dark reaction stage in TC solution, the crystalline phase of b-TiO$_2$ remains unchanged. However, the formation of a new crystalline phase is found as the Fe^0 crystalline phase disappeared, and its diffraction peaks at $2\theta = 30.2°, 35.7°, 57.3°, 62.9°, 87.2°$ are highly corresponding to (206), (119), (1115), (4012), (6212) crystal planes of Fe$_2$O$_3$ (JCPDS No.25–1402). This result means that an oxide layer of Fe$_2$O$_3$ on the Fe^0 surface is formed in the dark reaction. Fe 2p XPS spectra and TEM were also employed to confirm the formation of the oxide layer during the dark reaction. For Fe@Ti-2 (Fig. 3B), the peak at 706.62 eV is attributed to Fe^0, and the peaks at 724.33 eV and 710.82 eV are corresponded to Fe$_2$O$_3$, indicating that the surface of Fe^0 is covered by a thin layer of Fe$_2$O$_3$, which is consistent with the previous reports [6,14,40]. After 30 min of dark reaction, the peaks at 724.96 eV and 711.24 eV still exist, however, the characteristic peak of Fe^0 disappears, which further proves that the thickness of the oxide layer (Fe$_2$O$_3$) has increased significantly. The TEM image of Fig. 3C once again verifies the existence of a thin layer of Fe$_2$O$_3$ on the fresh catalyst, and the lattice spacings of about 0.20 nm and 0.25 nm are corresponded to the (110) crystal plane of Fe^0 (JCPDS No.06–0696) and (119) crystal plane of Fe$_2$O$_3$ (JCPDS No.25–1402). After 30 min of dark reaction (Fig. 3D), the average thickness of the passivation layer of Fe$_2$O$_3$ changes from 2.9537 nm to 9.7946 nm, which confirms the results of XRD and XPS.

Substantial researches have shown that under aerobic conditions, Fe^0 tends to be oxidized to form a passivation layer on its surface [30,31]. In this case, the contact between Fe^0 and pollutants is blocked by the passivation layer, resulting in the weakening of the catalytic performance of Fe^0-based catalysts and further drastical decline in the degradation efficiency of pollutants [32–34]. However, based on reverse thinking, this research intends to actively utilize the passivation layer instead of abandoning it. Therefore, starting from the thinking of constructing a heterojunction, the passivation layer of Fe$_2$O$_3$ is expected to be used as a semiconductor to cooperate with b-TiO$_2$ with unchanged crystal phase to form a heterojunction, achieving enhanced photocatalytic degradation of TC in the visible-light reaction stage.

3.2. Photocatalytic performance

Under visible-light irradiation, the photodegradation efficiency of TC was investigated using the as-synthesized materials. From Fig. 4A, it can be seen that the TC content remains unchanged after dark conditions for 30 min and even visible-light irradiation for 45 min, indicating TC is stable extremely and hard to be degraded naturally by visible-light. As for pristine Fe^0 and b-TiO$_2$, 80.51% and 37.50% of removal efficiency is obtained within 75 min, respectively. The removal efficiencies of TC reach 81.08%, 89.19% and 83.61% under 45 min of visible light irradiation using Fe@Ti-1, Fe@Ti-3 and Fe^0+b-TiO$_2$, respectively, and Fe@Ti-2 (only 7 mg dosage) exhibits the highest photocatalytic

performance of 98.67% within only 30 min. Obviously, compared to pristine Fe^0 and b-TiO$_2$, these composites obtain enhanced photodegradation efficiency. It can be supposed that a synergistic effect is induced by the combination of two materials, which means strong adsorption and reduction ability of Fe^0 and excellent photocatalytic ability of b-TiO$_2$ are integrated organically. Note that, the high photodegradability of Fe@Ti-2 is not only attributed to the strong reduction of Fe^0, but more significantly, it should be responsible for b-TiO$_2$ with fluffy sponge-like structure, which guarantees the high exposure of Fe^0 active sites, and also mitigates the negative impact of the passivation layer through formation of a Z-scheme heterojunction (as demonstrated in Section 3.3). Moreover, the photodegradation efficiency of Fe^0@b-TiO$_2$ is compared with that of photocatalysts reported in other literatures [24,45–52]. It can be deduced from Table 1 that at a lower catalyst dose and a higher TC concentration, a competitive photocatalytic performance is demonstrated within a shorter irradiation time. It is adequately illustrates that Fe^0@b-TiO$_2$ is an ideal material for the efficient treatment of tetracycline wastewater.

The structural destruction of TC and the formation of intermediates were confirmed by UV–vis absorption spectra using Fe@Ti-2. As explicated in Fig. 4B, the characteristic absorption peak of TC at 357 nm gradually weakens and finally disappears with the degradation reaction proceeds, which is ascribed to the complete degradation of TC and the exhaustive destruction of its structure. At the same time, a trend of first increasing and then decreasing is observed within a absorption band from 190 nm to 240 nm, indirectly showing the formation and degradation of intermediates [53].

The pseudo-first-order kinetics model is usually used for the kinetic analysis of TC photodegradation under visible-light irradiation [53]. As depicted in Fig. 4C, a significant linear correlation ($R^2 > 0.9$) is observed between $\ln(C/C_0)$ and irradiation time t, indicating a good fitting relationship between the two factors. Moreover, the absolute value of slope in the degradation fitted line of Fe@Ti-2 is much larger than that of other materials. From Fig. 4D, the photodegradation kinetics of TC over various materials are quantified with the reaction rate constant k. Generally, the composites have a higher k value compared with the single component. In detail, the k value of Fe@Ti-2 ($k = 0.0721$ min^{-1}) is approximately 4.71, 5.30 and 20.03 times as high as that of Fe@Ti-1 ($k = 0.0153$ min^{-1}), Fe@Ti-3 ($k = 0.0136$ min^{-1}) and pristine b-TiO$_2$ ($k = 0.0036$ min^{-1}), respectively. This result supports the idea that an improved photocatalytic activity of b-TiO$_2$ is obtained through the doping of Fe^0.

However, in the dark reaction stage, the removal of TC by Fe^0-containing materials mainly includes two stages, adsorption and chemical reduction. The adsorption is derived from the large specific surface area and abundant channels of Fe^0@b-TiO$_2$ composites, and the chemical reduction is triggered by the strong reduction ability of Fe^0. It may be concluded that the pseudo-first-order kinetics model is not suitable for the degradation of TC using Fe^0-based materials under dark conditions. Therefore, a modified kinetics model that takes both adsorption and chemical reduction processes into account is constructed for the removal
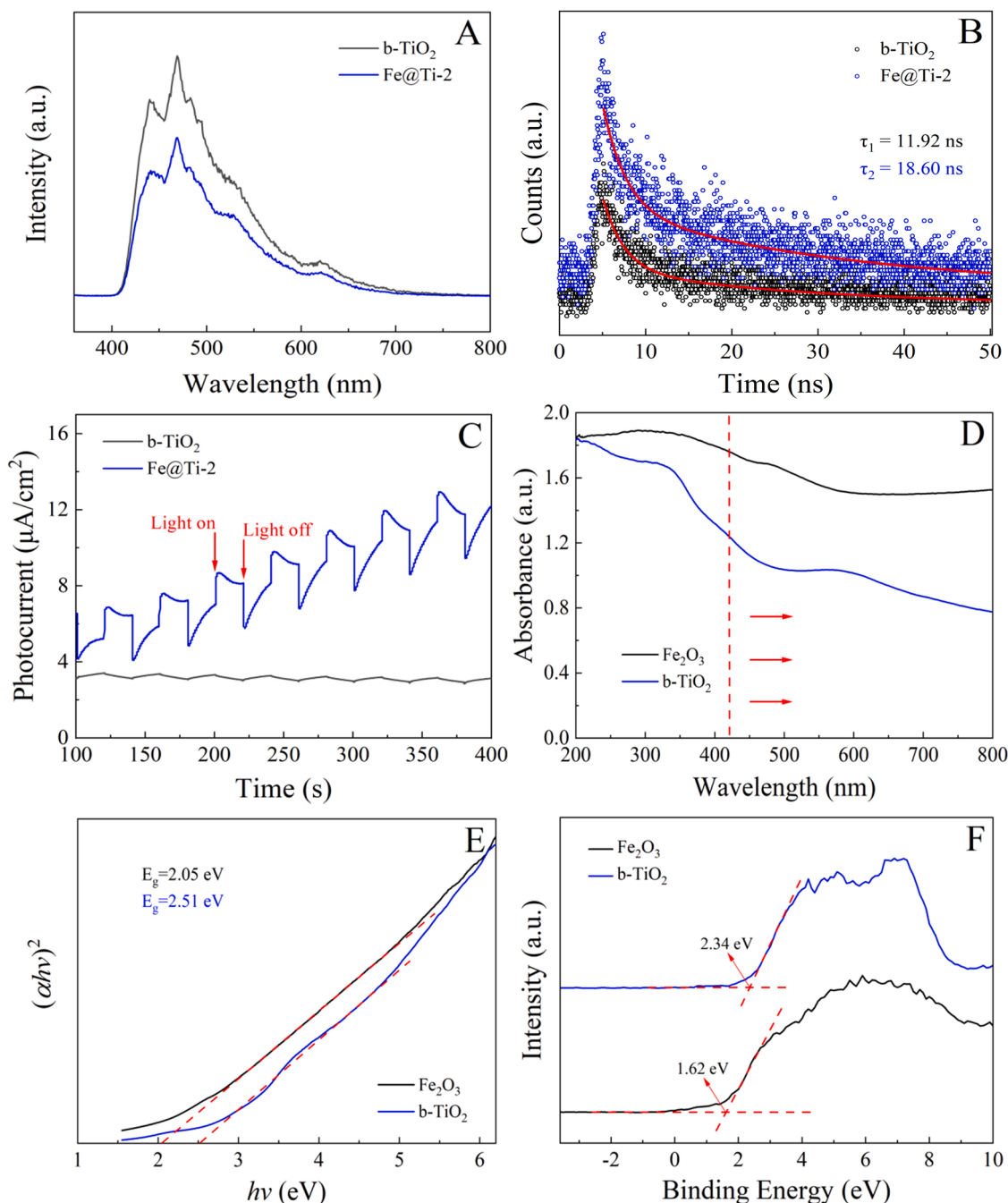
Fig. 5. (A) PL spectra, (B) time-resolved fluorescence spectra, (C) transient photocurrent responses of b-TiO$_2$ and Fe@Ti-2. (D) UV–vis DRS, (E) Tauc plots and (F) VB-XPS spectra of Fe$_2$O$_3$ and b-TiO$_2$.

of TC in the absence of light as reported by our group previously [53,54]. The equation is shown below:

$$C_{eq} / C_{ini} = \alpha \times \exp(-k_a \times k_r \times t) + (1-\alpha) \times \exp(-k_r \times t) \qquad (2)$$

where C_{ini} stands for the initial concentration of TC and C_{eq} represents the concentration of TC at reaction time t (min); α and $1-\alpha$ denote the weight values of adsorption and chemical reduction stages, respectively; k_a and k_r are the rate constants of adsorption and chemical reduction, respectively. As displayed in Fig. 4E, the R^2 values of all fitting curves are above 0.99, indicating that the removal behavior of TC on Fe^0-based materials under dark conditions can be well explained with the modified kinetics model. Specifically, the k_a values of Fe^0@b-TiO$_2$ composites are larger than that of pristine Fe^0, which proves that the existence of b-TiO$_2$

greatly ameliorated the adsorption capacity of Fe^0. In addition, the k_r values of these materials exhibit the following order: Fe@Ti-2 > Fe@Ti-3 > Fe@Ti-1, revealing that the increase of Fe^0 loading is beneficial to the improved activity for the composites. Nevertheless, excessive Fe^0 conversely leads to a decrease in the number of exposed active sites due to large accumulation of Fe^0 particles.

From the photocatalytic kinetics and dark reaction kinetics discussed above, it can be seen that the enhanced photocatalytic and reduction capabilities of Fe^0@b-TiO$_2$ are originated from the mutual stimulation between Fe^0 and b-TiO$_2$. That is, the loading of Fe^0 improves the photocatalytic performance of b-TiO$_2$ due to the promotion of photoelectron transfer and the inhibition of photo-generated electron-hole pairs recombination. Additionally, the doping of b-TiO$_2$ leads to a high degree of dispersion among Fe^0 particles, and the formation of a heterojunction

helps to prevent the reduction and photocatalytic reaction from being blocked by the passivation layer.

The stability and recyclability of materials are two essential indicators in practical applications. Given this, a 5-cycle of TC photodegradation experiment with Fe@Ti-2 was carried out. As plotted in Fig. 4F, compared with fresh samples, no palpable deterioration of TC degradation ability is captured for regenerated samples even after 5 cycles. Moreover, after regeneration and purification with a small amount of KBH_4 and UPW, the residual pollutants attached to Fe@Ti-2 are washed into the contaminated water, where Fe@Ti-2 can be easily separated and recycled using a magnetic field due to its magnetism with a saturation magnetization of 25.45 emu/g (Fig. S1). Therefore, our results have provided the necessary inspiration and guidance for the development and application prospect of $Fe^0@b-TiO_2$ in environmental remediation in view of its excellent stability and inherent magnetism.

3.3. Optical properties

The optical properties of photocatalysts are the key factors affecting its photodegradation performance. The recombination rate of photogenerated electron-hole pairs was investigated by PL spectroscopy. As shown in Fig. 5A, a high intensity emission peak is detected in the PL spectrum of pristine $b-TiO_2$, which means a large number of electrons (e^-) and holes (h^+) are combined. Compared with the emission peak of pure $b-TiO_2$, a weaker intensity emission peak of Fe@Ti-2 is detected. It can be inferred that more electron-hole trapping sites are provided owing to the cooperation of Fe^0 and $b-TiO_2$, which ensures the efficient separation of photo-generated electron-hole pairs [45]. The time-resolved fluorescence spectra after nonlinear fitting with a

multi-exponential decay function were used to measure the lifetime of photo-excited charges in photocatalysts. It can be seen from Fig. 5B that the average lifetime of charges in Fe@Ti-2 ($\tau_2 = 18.60$ ns) is longer than that of pristine $b-TiO_2$ ($\tau_1 = 11.92$ ns). The prolonged average lifetime demonstrates that efficient electron-hole pairs separation and accelerated charge transfer capability are obtained by Fe@Ti-2, meaning enhanced photodegradation of TC [50,55].

Transient photocurrent response is another important parameter for investigating the optical performance of photocatalysts. As plotted in Fig. 5C, the photocurrent response intensity of pure $b-TiO_2$ is quite low during multiple on-off cycles of visible-light irradiation, which may be due to the rapid recombination of photo-excited e^- and h^+. In contrast, a significant transient photocurrent response on Fe@Ti-2 is obtained, which is attributed to the generation of an internal electric field between Fe^0 and $b-TiO_2$. The formation of this electric field not only lays the foundation for the construction of a heterojunction between Fe_2O_3 and $b-TiO_2$, but also improves the mobility of photo-generated carriers, furthermore, realizes efficient photocatalytic degradation of TC [5]. This conclusion is also supported by the results of PL and time-resolved fluorescence spectra. Notably, the gradually increasing photocurrent response over time also indirectly indicates that a heterojunction with enhanced electron conductivity and mobility is constructed in-situ with the gradual formation of the passivation layer.

The light absorption range of samples was determined by UV–vis DRS to grasp their ability to absorb visible-light. As illustrated in Fig. 5D, based on promoted electron transfer due to the narrow band gap, an excellent visible-light absorption capacity of Fe_2O_3 produced after the dark reaction is achieved. Surprisingly, the light absorption range of $b-TiO_2$ covers the UV and visible-light regions. As described in many
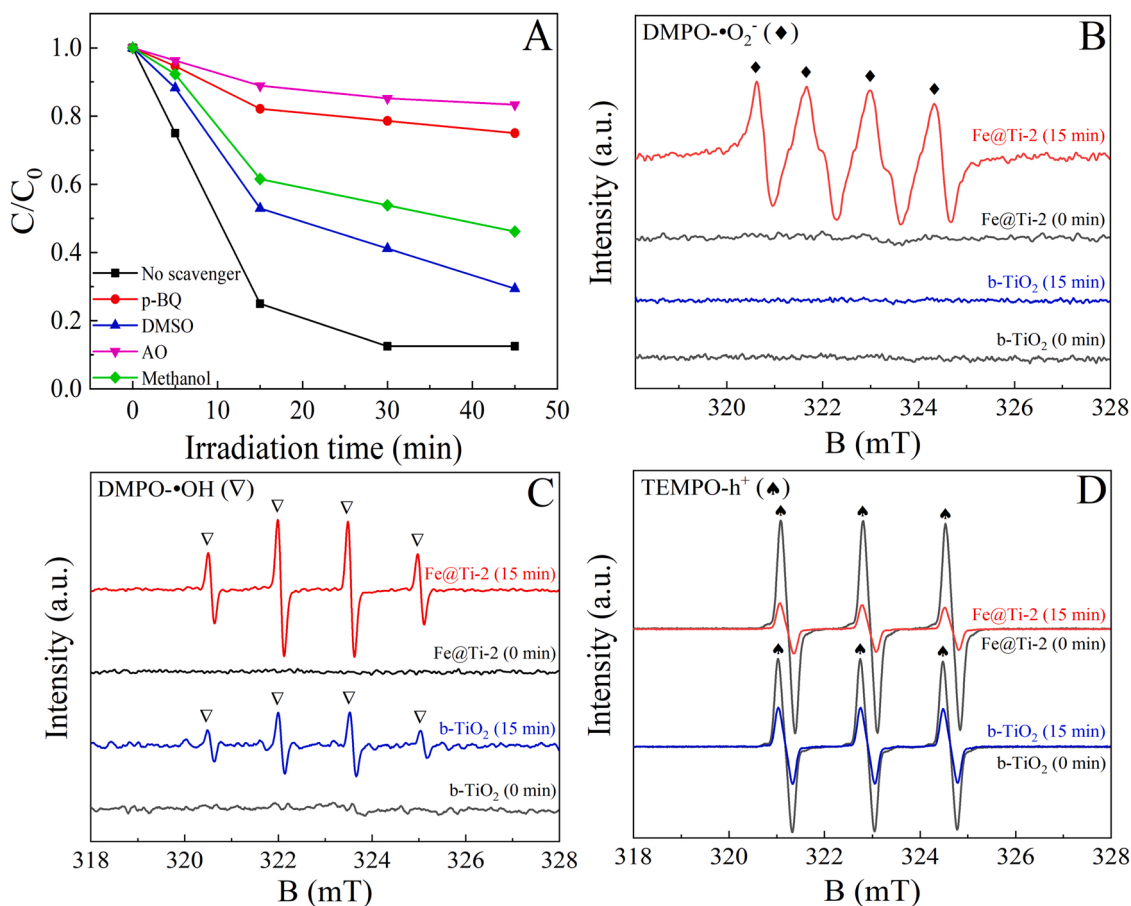

Fig. 6. (A) Free radical trapping experiments of TC photodegradation over Fe@Ti-2. ESR spectra of Fe@Ti-2 for (B) DMPO-•O_2^-, (C) DMPO-•OH and (D) TEMPO-h^+, respectively.
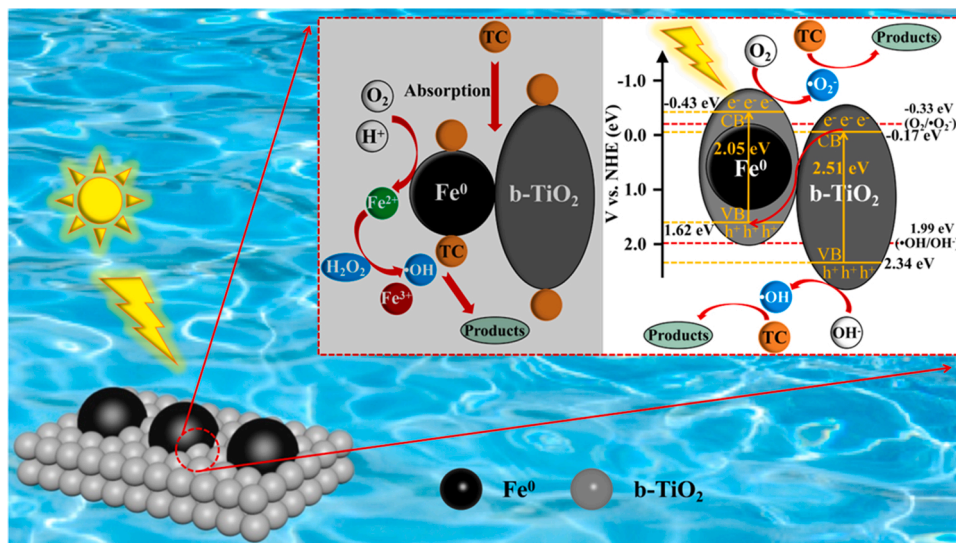
Fig. 7. The possible mechanism for TC degradation over Fe@Ti-2.

previous literatures, white TiO_2 has a strong light absorption only in the UV region ($\lambda < 420$ nm), while the light absorption of black TiO_2 is extended from UV to visible-light [52,56,57]. The excellent visible-light absorption ability of b-TiO_2 is stemmed from the generation of Ti^{3+} defects or OVs in the bulk phase during its preparation, which may substantially enhance the visible-light photodegradation activity of TC [27–29].

In order to verify the heterojunction structure of the photocatalyst during the photoreaction process, the band gap and VB of Fe_2O_3 and b-TiO_2 were calculated by Tauc plots and VB-XPS spectra respectively [58]. Moreover, the conduction band (CB) of materials was calculated based on their band gap energy and VB. Fig. 5E is derived from the conversion of the UV–vis DRS (Fig. 5D) based on the functional relationship between $(\alpha h\nu)^2$ and $h\nu$. The intersection of the tangent and x-axis represents the band gap energies of the materials after the tangent of the curves is obtained. From Fig. 5E, it can be deduced that the band gap energies of Fe_2O_3 and b-TiO_2 are 2.05 eV and 2.51 eV, respectively. Compared with white TiO_2, the narrower band gap of b-TiO_2 facilitates faster excitation of electrons from VB to CB, revealing enhanced photocatalytic ability of b-TiO_2. The VB of materials was analyzed by the VB-XPS spectra. As depicted in Fig. 5F, the valence band energies of Fe_2O_3 and b-TiO_2 are 1.62 eV and 2.34 eV, respectively. According to $E_g = E_{VB} - E_{CB}$ (where E_g represents band gap energy, E_{VB} and E_{CB} are valence band energy and conduction band energy respectively), the conduction band energies of Fe_2O_3 and b-TiO_2 are calculated as - 0.43 eV and - 0.17 eV, respectively [58]. Thus, in view of the VB and CB positions of the two components, it can be concluded that there are two possible heterojunction structures (type II and Z-scheme) for the enhanced visible-light degradation of TC.

Hence, a reasonable heterojunction structure urgently needs to be determined based on the above results and the conclusions of Section 3.4. Evidently, after the Fe_2O_3/b-TiO_2 heterojunction is irradiated by visible-light, the excited electrons in the two components transfer from their VB to CB, leaving holes in the VB at the same time. In the case of the type II heterojunction, the electrons in the CB of Fe_2O_3 can migrate to that of b-TiO_2. On the contrary, the holes in the VB of b-TiO_2 move to that of Fe_2O_3 to guarantee the effective separation of electrons and holes. In Section 3.4, the free radical trapping experiments and ESR analysis prove that superoxide radicals ($\bullet O_2^-$) and hydroxyl radicals ($\bullet OH$) are the main ROS. However, the CB of b-TiO_2 (- 0.17 eV) is more positive relative to the redox potential of $O_2/\bullet O_2^-$ (- 0.33 eV), and O_2 can not be reduced to $\bullet O_2^-$ by e^- in the CB of b-TiO_2 [45,59]. Meanwhile, the VB of Fe_2O_3 (1.62 eV) is more negative than the redox potential of

$\bullet OH/OH^-$ (1.99 eV) and $\bullet OH/H_2O$ (2.27 eV), as a result, the holes on it can not oxidize OH^-/H_2O to produce $\bullet OH$ for degradation of TC [60]. Obviously, this inference is inconsistent with the conclusion proved in Section 3.4, confirming that the type II structure is unreasonable. From the perspective of the Z-scheme heterojunction, the CB of Fe_2O_3 (- 0.43 eV) is more negative compared with - 0.33 eV of $E(O_2/\bullet O_2^-)$, and the electrons with strong reduction on it can reduce O_2 to $\bullet O_2^-$ [45,59]. Simultaneously, the VB of b-TiO_2 (2.34 eV) is more positive than 1.99 eV of $E(\bullet OH/OH^-)$ and 2.27 eV of $E(\bullet OH/H_2O)$, and the holes in the VB of b-TiO_2 are enough to oxidize OH^- and H_2O to generate $\bullet OH$ [59, 60]. In this case, after the composite material is excited by visible-light, the electrons in the CB of b-TiO_2 will combine with the holes in the VB of Fe_2O_3, and the electrons in the CB of Fe_2O_3 and the holes in the VB of b-TiO_2 are efficiently separated. Subsequently, these separated e^- and h^+ convert O_2 and OH^- into $\bullet O_2^-$ and $\bullet OH$, respectively, to achieve high-efficiency visible-light photodegradation of TC. The above results and discussions provide strong evidence that a Z-scheme heterojunction is built between Fe_2O_3 and b-TiO_2, which is a key factor for enhanced TC photocatalytic activity.

3.4. Photocatalytic mechanism and pathways

A series of free radical trapping experiments were carried out to deeply explore the effect of different active species ($\bullet O_2^-$, $\bullet OH$, e^-, h^+) on the photodegradation of TC, and to further clarify the photocatalytic mechanism of TC over Fe@Ti-2. Herein, a variety of additives such as p-BQ, DMSO, AO and methanol were adopted as quenchers for $\bullet O_2^-$, e^-, h^+, and $\bullet OH$, respectively [53]. As presented in Fig. 6A, an 87.50% of TC photodegradation rate is achieved in the visible-light irradiation stage, and the addition of p-BQ, DMSO, AO and methanol slows down the photodegradation rate of TC by 57.95%, 28.68%, 72.69% and 41.35%, respectively, and the order of the inhibitory effect of AO > p-BQ > methanol > DMSO is obtained. It can be inferred that the presences of $\bullet O_2^-$, e^-, h^+ and $\bullet OH$ have a positive effect on the photocatalytic efficiency of TC over Fe@Ti-2. Among them, h^+, $\bullet O_2^-$ and $\bullet OH$ are the main active species and e^- as the secondary active species.

ESR technology was employed to measure the production of ROS and h^+ during TC degradation over b-TiO_2 and Fe@Ti-2. As shown in Fig. 6B, no signals are found in dark conditions with b-TiO_2 and Fe@Ti-2. After 15 min of visible-light irradiation, 4 remarkable characteristic peaks related to $\bullet O_2^-$ with intensity ratio of 1:1:1:1 can only be detected in Fe@Ti-2, indicating the generation of abundant $\bullet O_2^-$ during the photocatalytic of TC over Fe@Ti-2. Conversely, $\bullet O_2^-$ cannot be generated in b-
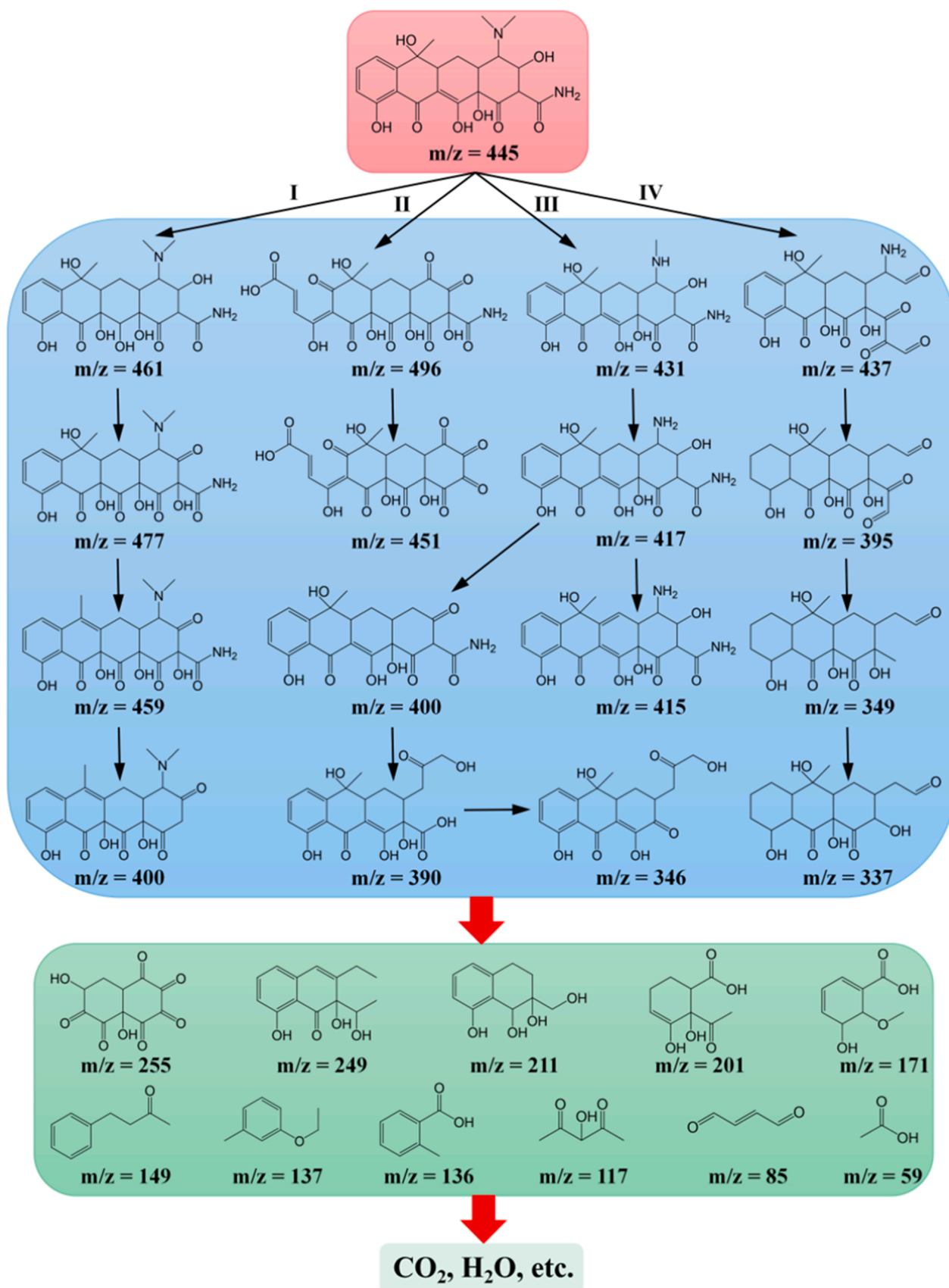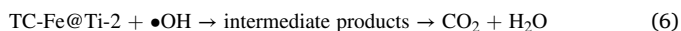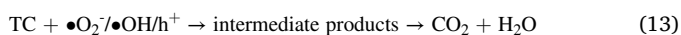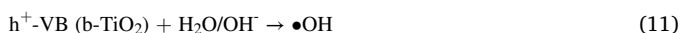
Fig. 8. Proposed pathways for TC photodegradation over Fe@Ti-2.

TiO$_2$ due to the more positive CB (- 0.17 eV) relative to the redox potential of O$_2$/•O$_2^-$ (- 0.33 eV), as demonstrated in Section 3.3. Furthermore, 4 notable •OH characteristic peaks (Fig. 6C) with intensity distribution of 1:2:2:1 are captured using b-TiO$_2$ and Fe@Ti-2 under visible-light irradiation for 15 min, compared with no characteristic peaks in dark conditions, once more confirming the formation of •OH in the TC photodegradation process [53,54]. The intensity of the characteristic peaks of •OH generated by Fe@Ti-2 is significantly higher than that generated by b-TiO$_2$, indicating an increase in the production of highly reactive •OH after Fe^0 loading. Similar results are also confirmed in the ESR test of h$^+$ (Fig. 6D). After 15 min of visible-light irradiation, the weakening of the intensity of the characteristic peaks in Fe@Ti-2 is more than that in b-TiO$_2$, reflecting the more effective separation and utilization of h$^+$ in Fe@Ti-2 than that in b-TiO$_2$. The conclusion of ESR analysis is in accordance with that of free radical trapping experiments.

A schematic representation illustrating the possible mechanism of TC degradation over Fe@Ti-2 is displayed in Fig. 7. Our findings highlight that the whole degradation of TC over Fe@Ti-2 is divided into two stages: chemical reduction and further photocatalytic reaction. Under darkness, the chemical reduction of Fe^0 plays a key role in TC removal, and the presence of b-TiO$_2$ support further enhances its reduction ability due to the exposure of more active sites by inhibiting aggregation between Fe^0 particles [61]. At the beginning, TC is gradually adsorbed on Fe@Ti-2 and ultimately reaches an adsorption-desorption equilibrium; subsequently, Fe^0 is reacted with oxygen in the contaminated water to form iron ions and H$_2$O$_2$, which contribute to the formation of •OH with the Fenton-like reaction; finally, the TC adsorbed on the material reacts with •OH to generate intermediates, even CO$_2$ and H$_2$O (Eqs. (3) - (6)).

$$Fe@Ti\text{-}2 + TC \rightarrow TC\text{-}Fe@Ti\text{-}2 \tag{3}$$

$$Fe^0 + O_2 + 2H^+ \rightarrow Fe^{2+} + H_2O_2 \tag{4}$$

$$Fe^{2+} + H_2O_2 \rightarrow Fe^{3+} + \bullet OH + OH^- \tag{5}$$

$$TC\text{-}Fe@Ti\text{-}2 + \bullet OH \rightarrow intermediate\ products \rightarrow CO_2 + H_2O \tag{6}$$

However, under visible-light irradiation, the degradation of TC is dominated by the photocatalytic properties of Fe@Ti-2 [61–63]. Thoroughly, the electrons on Fe$_2$O$_3$ and b-TiO$_2$ are firstly transferred from the VB to CB after visible-light excitation. Then, the electrons in the CB of b-TiO$_2$ are transferred to the VB of Fe$_2$O$_3$ and recombined with the free holes on it. At the same time, the strong reduction electrons in the CB of Fe$_2$O$_3$ can react with O$_2$ to form •O$_2^-$, and the holes in the VB of b-TiO$_2$ may indirectly convert H$_2$O and OH$^-$ into •OH owing to more positive VB of b-TiO$_2$ (2.34 eV) relative to the redox potential of •OH/H$_2$O (2.27 eV) and •OH/OH$^-$ (1.99 eV) [60]. After that, the Fe^{3+} produced during dark reaction may react with electrons to form Fe^{2+}, which apparently facilitates the cycle between Fe^{2+} and Fe^{3+}, ensuring an excellent stability of Fe@Ti-2. Moreover, the generated holes can involve directly in the photodegradation of TC attributing to its strong oxidation. Finally, TC will be decomposed into CO$_2$ and H$_2$O by produced •O$_2^-$, •OH and h$^+$. The corresponding photodegradation mechanism of TC can be described with Eqs. (7) - (13).

$$Fe_2O_3 + h\nu \rightarrow h^+ + e^- \tag{7}$$

$$b\text{-}TiO_2 + h\nu \rightarrow h^+ + e^- \tag{8}$$

$$e^-\text{-}CB\ (b\text{-}TiO_2) \rightarrow h^+\text{-}VB\ (Fe_2O_3) \tag{9}$$

$$e^-\text{-}CB\ (Fe_2O_3) + O_2 \rightarrow \bullet O_2^- \tag{10}$$

$$h^+\text{-}VB\ (b\text{-}TiO_2) + H_2O/OH^- \rightarrow \bullet OH \tag{11}$$

$$Fe^{3+} + e^- \rightarrow Fe^{2+} \tag{12}$$

$$TC + \bullet O_2^-/\bullet OH/h^+ \rightarrow intermediate\ products \rightarrow CO_2 + H_2O \tag{13}$$

The degradation products of TC in different time periods under visible-light conditions were identified and analyzed by LC-MS based on their mass-to-charge ratio (m/z). According to the recognition results of the MS spectra shown in Fig. S2, the possible paths of TC photodegradation over Fe@Ti-2 are summarized in Fig. 8 [51,58,64–66].

In detail, TC (m/z = 445) first undergoes two hydroxylation reactions to generate m/z = 461 and m/z = 477 respectively in pathway I. Then, a dehydration step (m/z = 459) and a deamidation step (m/z = 400) are recorded successively. In the case of pathway II, m/z = 496 is produced after the ring opening and N-demethylation steps of TC. Afterwards, it is oxidized to m/z = 451. In pathway III, TC is converted to m/z = 417 after two demethylation processes. On the one hand, it further forms m/z = 415 with a dehydrogenation step. On the other hand, it generates m/z = 400 under a deamination process, which subsequently leads to the production of m/z = 346 due to the ring opening, deamination and dehydroxylation processes. As for pathway IV, the formation of m/z = 437 is induced by the demethylation and ring opening of TC. Immediately afterwards, m/z = 349 is produced after two decarbonylation processes. Furthermore, m/z = 337 is generated with a demethylation step. It can also be seen from the figure that some intermediates with medium molecular weight, such as m/z = 255, 249, 211, etc., and even some small molecule products, such as m/z = 85, 59, etc. are identified, reflecting further degradation of the intermediates generated by the above four paths. Eventually, these substances with small molecular weight will be decomposed into harmless CO$_2$ and H$_2$O, etc. Notably, under the four pathways involved in TC degradation, hydroxylation, ring opening and N-demethylation may originate from attack of •OH, •O$_2^-$ and h$^+$, respectively. These results again demonstrate the key role of the three active species in the photodegradation of TC, as pointed out in the free radical trapping experiments.

4. Conclusions

A novel recyclable Fe^0@b-TiO$_2$ Z-scheme heterojunction catalyst with high photocatalytic performance was successfully synthesized. The excellent TC degradation activity and stability of Fe@Ti-2 were ascribed to two aspects: the strong reduction ability of highly dispersed Fe^0 and the in-situ construction of a Z-scheme heterojunction. The high dispersion of Fe^0 was induced by b-TiO$_2$ and was confirmed by SEM, mapping and XRD. The formation of Fe$_2$O$_3$ crystalline phase after the dark reaction was observed, and combined with the band structure of Fe$_2$O$_3$ and b-TiO$_2$, it can be concluded that a Z-scheme heterojunction was formed in-situ during the dark reaction. The heterojunction improved the migration rate of photo-generated carriers and significantly suppressed their recombination, resulting in enhanced photodegradation efficiency of TC. Furthermore, the photodegradation of TC originated from the action of ROS (•O$_2^-$, •OH) and h$^+$ generated during visible-light irradiation, which ultimately induced the decomposition of TC and its intermediates. This work proposes a new mechanism of innovatively activating the passivation layer on the surface of Fe^0 as semiconductor to construct a Z-scheme heterojunction in-situ for high-efficiency environmental remediation.

CRediT authorship contribution statement

Xi Wu: Conceptualization, Methodology, Writing – original draft. **Xiangyu Wang**: Data curation, Supervision, Writing – review & editing. **Yu Xie**: Writing – review & editing, Methodology. **Nanqi Ren**: Writing – review & editing, Resources. **Jun Ma**: Writing – review & editing. **Ping Ning**: Writing – review & editing.

Declaration of Competing Interest

The authors declare that they have no known competing financial interests or personal relationships that could have appeared to influence the work reported in this paper.

Acknowledgements

Appendix A. Supporting information

Supplementary data associated with this article can be found in the online version at doi:10.1016/j.apcatb.2022.121325.

References

[1] W. Shi, F. Guo, S. Yuan, In situ synthesis of Z-scheme Ag_3PO_4/$CuBi_2O_4$ photocatalysts and enhanced photocatalytic performance for the degradation of tetracycline under visible light irradiation, Appl. Catal. B: Environ. 209 (2017) 720–728.

[2] J. Lyu, Z. Zhou, Y. Wang, J. Li, Q. Li, Y. Zhang, X. Ma, J. Guan, X. Wei, Platinum-enhanced amorphous TiO_2-filled mesoporous TiO_2 crystals for the photocatalytic mineralization of tetracycline hydrochloride, J. Hazard. Mater. 373 (2019) 278–284.

[3] Y. Zhou, Y. Gao, J. Jiang, Y.M. Shen, S.Y. Pang, Z. Wang, J. Duan, Q. Guo, C. Guan, J. Ma, Transformation of tetracycline antibiotics during water treatment with unactivated peroxymonosulfate, Chem. Eng. J. 379 (2020) 122378.

[4] B. Chen, L. Lin, L. Fang, Y. Yang, E. Chen, K. Yuan, S. Zou, X. Wang, T. Luan, Complex pollution of antibiotic resistance genes due to beta-lactam and aminoglycoside use in aquaculture farming, Water Res. 134 (2018) 200–208.

[5] Q. Zhu, Y. Sun, F. Na, J. Wei, S. Xu, Y. Li, F. Guo, Fabrication of CdS/titanium-oxo-cluster nanocomposites based on a Ti_{32} framework with enhanced photocatalytic activity for tetracycline hydrochloride degradation under visible light, Appl. Catal. B: Environ. 254 (2019) 541–550.

[6] Y. Shao, Y. Gao, Q. Yue, W. Kong, B. Gao, W. Wang, W. Jiang, Degradation of chlortetracycline with simultaneous removal of copper (II) from aqueous solution using wheat straw-supported nanoscale zero-valent iron, Chem. Eng. J. 379 (2020), 122384.

[7] M. Pirsaheb, S. Moradi, M. Shahlaei, X. Wang, N. Farhadian, A new composite of nano zero-valent iron encapsulated in carbon dots for oxidative removal of bio-refractory antibiotics from water, J. Clean. Prod. 209 (2019) 1523–1532.

[8] Y. Ma, X. Lv, D. Xiong, X. Zhao, Z. Zhang, Catalytic degradation of ranitidine using novel magnetic Ti_3C_2-based MXene nanosheets modified with nanoscale zero-valent iron particles, Appl. Catal. B: Environ. 284 (2021) 119720.

[9] Z. Li, Y. Sun, Y. Yang, Y. Han, T. Wang, J. Chen, D.C.W. Tsang, Biochar-supported nanoscale zero-valent iron as an efficient catalyst for organic degradation in groundwater, J. Hazard. Mater. 383 (2020) 121240.

[10] X. Luo, X. Guo, X. Xia, X. Zhang, N. Ma, S. Leng, S. Ullah, Z.M. Ayalew, Rapid and long-effective removal of phosphate from water by zero-valent iron in combination with hypochlorite (ZVI/NaClO), Chem. Eng. J. 382 (2020) 122835.

[11] S. Giri, M. Bhaumik, R. Das, V.K. Gupta, A. Maity, Dehalogenation of aromatic halides by polyaniline/zero-valent iron composite nanofiber: Kinetics and mechanisms, Appl. Catal. B: Environ. 202 (2017) 207–216.

[12] X. Wang, A. Wang, J. Ma, M. Fu, Facile green synthesis of functional nanoscale zero-valent iron and studies of its activity toward ultrasound-enhanced decolorization of cationic dyes, Chemosphere 166 (2017) 80–88.

[13] C. Shan, M. Tong, Efficient removal of trace arsenite through oxidation and adsorption by magnetic nanoparticles modified with Fe-Mn binary oxide, Water Res. 47 (2013) 3411–3421.

[14] J. Xu, X. Wang, F. Pan, Y. Qin, J. Xia, J. Li, F. Wu, Synthesis of the mesoporous carbon-nano-zero-valent iron composite and activation of sulfite for removal of organic pollutants, Chem. Eng. J. 353 (2018) 542–549.

[15] L. Zhu, L. Tong, N. Zhao, J. Li, Y. Lv, Coupling interaction between porous biochar and nano zero valent iron/nano α-hydroxyl iron oxide improves the remediation efficiency of cadmium in aqueous solution, Chemosphere 219 (2019) 493–503.

[16] X. Wang, M. Zhu, H. Liu, J. Ma, F. Li, Modification of Pd-Fe nanoparticles for catalytic dechlorination of 2,4-dichlorophenol, Sci. Total Environ. 449 (2013) 157–167.

[17] X. Ruan, H. Liu, X. Ning, D. Zhao, X. Fan, Screening for the action mechanisms of Fe and Ni in the reduction of Cr(VI) by Fe/Ni nanoparticles, Sci. Total Environ. 715 (2020), 136822.

[18] L. Xu, L. Zhao, Y. Mao, Z. Zhou, D. Wu, Enhancing the degradation of bisphenol A by dioxygen activation using bimetallic Cu/Fe@zeolite: critical role of Cu(I) and superoxide radical, Sep. Purif. Technol. 253 (2020) 117550.

[19] Z. Du, K. Li, S. Zhou, X. Liu, Y. Yu, Y. Zhang, Y. He, Y. Zhang, Degradation of ofloxacin with heterogeneous photo-Fenton catalyzed by biogenic Fe-Mn oxides, Chem. Eng. J. 380 (2020) 122427.

[20] X. Li, J. Yu, M. Jaroniec, Hierarchical photocatalysts, Chem. Soc. Rev. 45 (2016) 2603–2636.

[21] D. Fattakhova-Rohlfing, A. Zaleska, T. Bein, Three-dimensional titanium dioxide nanomaterials, Chem. Rev. 114 (2014) 9487–9558.

[22] S.D. Perera, R.G. Mariano, K. Vu, N. Nour, O. Seitz, Y. Chabal, K.J. Balkus Jr., Hydrothermal synthesis of graphene-TiO_2 nanotube composites with enhanced photocatalytic activity, ACS Catal. 2 (2012) 949–956.

[23] X.D. Zhu, Y.J. Wang, R.J. Sun, D.M. Zhou, Photocatalytic degradation of tetracycline in aqueous solution by nanosized TiO_2, Chemosphere 92 (2013) 925–932.

[24] S. Wu, H. Hu, Y. Lin, J. Zhang, Y.H. Hu, Visible light photocatalytic degradation of tetracycline over TiO_2, Chem. Eng. J. 382 (2020), 122842.

[25] X. Chen, L. Liu, F. Huang, Black titanium dioxide (TiO_2) nanomaterials, Chem. Soc. Rev. 44 (2015) 1861–1885.

[26] T.S. Rajaraman, S.P. Parikh, V.G. Gandhi, Black TiO_2: a review of its properties and conflicting trends, Chem. Eng. J. 389 (2020), 123918.

[27] F. Zuo, L. Wang, T. Wu, Z. Zhang, D. Borchardt, P. Feng, Self-doped Ti^{3+} enhanced photocatalyst for hydrogen production under visible light, J. Am. Chem. Soc. 132 (2010) 11856–11857.

[28] A. Naldoni, M. Allieta, S. Santangelo, M. Marelli, F. Fabbri, S. Cappelli, C. L. Bianchi, R. Psaro, V.D. Santo, Effect of nature and location of defects on bandgap narrowing in black TiO_2 nanoparticles, J. Am. Chem. Soc. 134 (2012) 7600–7603.

[29] L. Li, Y. Chen, S. Jiao, Z. Fang, X. Liu, Y. Xu, G. Pang, S. Feng, Synthesis, microstructure, and properties of black anatase and B phase TiO_2 nanoparticles, Mater. Des. 100 (2016) 235–240.

[30] J. Xu, Y. Wang, C. Weng, W. Bai, Y. Jiao, R. Kaegi, G.V. Lowry, Reactivity, selectivity, and long-term performance of sulfidized nanoscale zerovalent iron with different properties, Environ. Sci. Technol. 53 (2019) 5936–5945.

[31] N. Sleiman, V. Deluchat, M. Wazne, M. Mallet, A. Courtin-Nomade, V. Kazpard, M. Baudu, Phosphate removal from aqueous solution using ZVI/sand bed reactor: Behavior and mechanism, Water Res. 99 (2016) 56–65.

[32] L. Tan, S. Lu, Z. Fang, W. Cheng, E.P. Tsang, Enhanced reductive debromination and subsequent oxidative ring-opening of decabromodiphenyl ether by integrated catalyst of nZVI supported on magnetic Fe_3O_4 nanoparticles, Appl. Catal. B: Environ. 200 (2017) 200–210.

[33] Y. Hu, X. Li, Influence of a thin aluminum hydroxide coating layer on the suspension stability and reductive reactivity of nanoscale zero-valent iron, Appl. Catal. B: Environ. 226 (2018) 554–564.

[34] Z. Cao, X. Liu, J. Xu, J. Zhang, Y. Yang, J. Zhou, X. Xu, G.V. Lowry, Removal of antibiotic florfenicol by sulfide-modified nanoscale zero-valent iron, Environ. Sci. Technol. 51 (2017) 11269–11277.

[35] H.Y. Wang, R. Hu, N. Wang, G.L. Hu, K. Wang, W.H. Xie, R. Cao, Boosting photoanodic activity for water splitting in carbon dots aqueous solution without any traditional supporting electrolyte, Appl. Catal. B: Environ. 296 (2021), 120378.

[36] J. Yu, X. Hou, X. Hu, H. Yuan, J. Wang, C. Chen, Efficient degradation of chloramphenicol by zero-valent iron microspheres and new insights in mechanisms, Appl. Catal. B: Environ. 256 (2019) 117876.

[37] Z. Chi, Z. Wang, Y. Liu, G. Yang, Preparation of organosolv lignin-stabilized nano zero-valent iron and its application as granular electrode in the tertiary treatment of pulp and paper wastewater, Chem. Eng. J. 331 (2018) 317–325.

[38] Q. Du, G. Li, S. Zhang, J. Song, Y. zhao, F. Yang, High-dispersion zero-valent iron particles stabilized by artificial humic acid for lead ion removal, J. Hazard. Mater. 383 (2020), 121170.

[39] Z. Li, S. Xu, G. Xiao, L. Qian, Y. Song, Removal of hexavalent chromium from groundwater using sodium alginate dispersed nano zero-valent iron, J. Environ. Manag. 244 (2019) 33–39.

[40] Z. Fang, X. Qiu, J. Chen, X. Qiu, Degradation of metronidazole by nanoscale zero-valent metal prepared from steel pickling waste liquor, Appl. Catal. B: Environ. 100 (2010) 221–228.

[41] Y.H. Hwang, D.G. Kim, H.S. Shin, Effects of synthesis conditions on the characteristics and reactivity of nano scale zero valent iron, Appl. Catal. B: Environ. 105 (2011) 144–150.

[42] S.S. Rezaei, B. Kakavandi, M. Noorisepehr, A.A. Isari, S. Zabih, P. Bashardoust, Photocatalytic oxidation of tetracycline by magnetic carbon-supported TiO_2 nanoparticles catalyzed peroxydisulfate: performance, synergy and reaction mechanism studies, Sep. Purif. Technol. 258 (2021), 117936.

[43] T. Zhang, Y. Liu, Y. Rao, X. Li, D. Yuan, S. Tang, Q. Zhao, Enhanced photocatalytic activity of TiO_2 with acetylene black and persulfate for degradation of tetracycline hydrochloride under visible light, Chem. Eng. J. 384 (2020) 123350.

[44] X. Yu, J. Huang, J. Zhao, S. Liu, D. Xiang, Y. Tang, J. Li, Q. Guo, X. Ma, J. Zhao, Efficient visible light photocatalytic antibiotic elimination performance induced by nanostructured Ag/AgCl@Ti^{3+}-TiO_2 mesocrystals, Chem. Eng. J. 403 (2021), 126359.

[45] F. Guo, W. Shi, M. Li, Y. Shi, H. Wen, 2D/2D Z-scheme heterojunction of $CuInS_2$/g-C_3N_4 for enhanced visible-light-driven photocatalytic activity towards the degradation of tetracycline, Sep. Purif. Technol. 210 (2019) 608–615.

[46] R. Li, W. Li, C. Jin, Q. He, Y. Wang, Fabrication of ZIF-8@TiO_2 micron composite via hydrothermal method with enhanced absorption and photocatalytic activities in tetracycline degradation, J. Alloy. Compd. 825 (2020), 154008.

[47] H. Yu, D. Ge, Y. Liu, Y. Lu, X. Wang, M. Huo, W. Qin, One-pot synthesis of BiOCl microflowers co-modified with Mn and oxygen vacancies for enhanced photocatalytic degradation of tetracycline under visible light, Sep. Purif. Technol. 251 (2020), 117414.

[48] F. Guo, X. Huang, Z. Chen, H. Sun, L. Chen, Prominent co-catalytic effect of CoP nanoparticles anchored on high-crystalline g-C_3N_4 nanosheets for enhanced visible-light photocatalytic degradation of tetracycline in wastewater, Chem. Eng. J. 395 (2020), 125118.

[49] F. Guo, W. Shi, H. Wang, M. Han, W. Guan, H. Huang, Y. Liu, Z. Kang, Study on highly enhanced photocatalytic tetracycline degradation of type II AgI/$CuBi_2O_4$ and Z-scheme AgBr/$CuBi_2O_4$ heterojunction photocatalysts, J. Hazard. Mater. 349 (2018) 111–118.

[50] W. Shi, F. Guo, H. Wang, M. Han, H. Li, S. Yuan, H. Huang, Y. Liu, Z. Kang, Carbon dots decorated the exposing high-reactive (111) facets CoO octahedrons with enhanced photocatalytic activity and stability for tetracycline degradation under visible light irradiation, Appl. Catal. B: Environ. 219 (2017) 36–44.

[51] L. Ren, W. Zhou, B. Sun, H. Li, P. Qiao, Y. Xu, J. Wu, K. Lin, H. Fu, Defects-engineering of magnetic γ-Fe$_2$O$_3$ ultrathin nanosheets/mesoporous black TiO$_2$ hollow sphere heterojunctions for efficient charge separation and the solar-driven photocatalytic mechanism of tetracycline degradation, Appl. Catal. B: Environ. 240 (2019) 319–328.

[52] S. Wu, X. Li, Y. Tian, Y. Lin, Y.H. Hu, Excellent photocatalytic degradation of tetracycline over black anatase-TiO$_2$ under visible light, Chem. Eng. J. 406 (2021), 126747.

[53] X. Wang, A. Wang, M. Lu, J. Ma, Synthesis of magnetically recoverable Fe^0/graphene-TiO$_2$ nanowires composite for both reduction and photocatalytic oxidation of metronidazole, Chem. Eng. J. 337 (2018) 372–384.

[54] X. Wang, M. Lu, J. Ma, P. Ning, Preparation of air-stable magnetic g-C$_3$N$_4$@Fe^0-graphene composite by new reduction method for simultaneous and synergistic conversion of organic dyes and heavy metal ions in aqueous solution, Sep. Purif. Technol. 212 (2019) 586–596.

[55] Q. Shi, Y. Zhang, D. Sun, S. Zhang, T. Tang, X. Zhang, S. Cao, Bi$_2$O$_3$-sensitized TiO$_2$ hollow photocatalyst drives the efficient removal of tetracyclines under visible light, Inorg. Chem. 59 (2020) 18131–18140.

[56] W. Hu, W. Zhou, K. Zhang, X. Zhang, L. Wang, B. Jiang, G. Tian, D. Zhao, H. Fu, Facile strategy for controllable synthesis of stable mesoporous black TiO$_2$ hollow spheres with efficient solar-driven photocatalytic hydrogen evolution, J. Mater. Chem. A 4 (2016) 7495–7502.

[57] Y. Chen, H. Yin, F. Li, J. Zhou, L. Wang, J. Wang, S. Ai, Polydopamine-sensitized WS$_2$/black-TiO$_2$ heterojunction for histone acetyltransferase detection with enhanced visible-light-driven photoelectrochemical activity, Chem. Eng. J. 393 (2020) 124707.

[58] A. Wang, Z. Zheng, H. Wang, Y. Chen, C. Luo, D. Liang, B. Hu, R. Qiu, K. Yan, 3D hierarchical H$_2$-reduced Mn-doped CeO$_2$ microflowers assembled from nanotubes as a high-performance Fenton-like photocatalyst for tetracycline antibiotics degradation, Appl. Catal. B: Environ. 277 (2020), 119171.

[59] P. Ning, H. Chen, J. Pan, J. Liang, L. Qin, D. Chen, Y. Huang, Surface defect-rich g-C$_3$N$_4$/TiO$_2$ Z-scheme heterojunction for efficient photocatalytic antibiotic removal: rational regulation of free radicals and photocatalytic mechanism, Catal. Sci. Technol. 10 (2020) 8295–8304.

[60] Z. Ma, L. Hu, X. Li, L. Deng, G. Fan, Y. He, A novel nano-sized MoS$_2$ decorated Bi$_2$O$_3$ heterojunction with enhanced photocatalytic performance for methylene blue and tetracycline degradation, Ceram. Int. 45 (2019) 15824–15833.

[61] X. Wang, Y. Xie, J. Ma, P. Ning, Facile assembly of novel g-C$_3$N$_4$@expanded graphite and surface loading of nano zero-valent iron for enhanced synergistic degradation of tetracycline, RSC Adv. 9 (2019) 34658–34670.

[62] N. Nasseh, L. Taghavi, B. Barikbin, M.A. Nasseri, Synthesis and characterizations of a novel FeNi$_3$/SiO$_2$/CuS magnetic nanocomposite for photocatalytic degradation of tetracycline in simulated wastewater, J. Clean. Prod. 179 (2018) 42–54.

[63] X. Liu, Y. Yang, H. Li, Z. Yang, Y. Fang, Visible light degradation of tetracycline using oxygen-rich titanium dioxide nanosheets decorated by carbon quantum dots, Chem. Eng. J. 408 (2021) 127259.

[64] C. Li, S. Yu, H. Che, X. Zhang, J. Han, Y. Mao, Y. Wang, C. Liu, H. Dong, Fabrication of Z-scheme heterojunction by anchoring mesoporous γ-Fe$_2$O$_3$ nanospheres on g-C$_3$N$_4$ for degrading tetracycline hydrochloride in water, ACS Sustain. Chem. Eng. 6 (2018) 16437–16447.

[65] J. Chen, X. Zhang, X. Shi, F. Bi, Y. Yang, Y. Wang, Synergistic effects of octahedral TiO$_2$-MIL-101(Cr) with two heterojunctions for enhancing visible-light photocatalytic degradation of liquid tetracycline and gaseous toluene, J. Colloid. Interface Sci. 579 (2020) 37–49.

[66] A. Kubiak, Z. Bielan, M. Kubacka, E. Gabała, A. Zgoła-Grześkowiak, M. Janczarek, M. Zalas, A. Zielińska-Jurek, K. Siwińska-Ciesielczyk, T. Jesionowski, Microwave-assisted synthesis of a TiO$_2$-CuO heterojunction with enhanced photocatalytic activity against tetracycline, Appl. Surf. Sci. 520 (2020), 146344.